Quantitative Single-Particle Fluorescence Imaging Elucidates Semiconductor Shell Influence on Ag@TiO$_2$ Photocatalysis

Yujie Liu, Kun Zhang, Xiaochaoran Tian, Lei Zhou,* Jianwei Liu,* and Baohong Liu*

Cite This: *ACS Appl. Mater. Interfaces* 2021, 13, 7680−7687

Read Online

ACCESS | Metrics & More | Article Recommendations | Supporting Information

ABSTRACT: The understanding of the structure−reactivity relationship is helpful for the nanocatalyst (NC) design. However, though precisely parse, this information is challenging due to the heterogeneity of NCs and the complex mechanism of energetic charge carrier (e$^-$/h$^+$ pairs) generation and transfer within the catalysts upon light irradiation. Here, the effect of the semiconductor shell on the photocatalytic redox reaction is probed at the single-Ag@TiO$_2$ NC level with single-molecule imaging. By engineering the TiO$_2$ shell thickness, catalytic activities of the NCs are precisely controlled and quantitatively measured to show a parabolic-like distribution with increasing TiO$_2$ thickness. Besides, the varied activity among different NCs and the dynamic activity fluctuation of single NCs during continuous redox conversion are observed. Mathematical analysis indicates that the TiO$_2$ layer affects the activity of the core−shell NCs by simultaneously affecting the fate of photo-induced e$^-$/h$^+$ pairs and hot electrons generated at the Ag core. This work sheds light on molecular-scale elucidation of the impact of metal−semiconductor NC structures on their reactivities.

KEYWORDS: Ag@TiO$_2$, energetic charge carriers, quantitative investigation, single-molecule imaging, semiconductor thickness
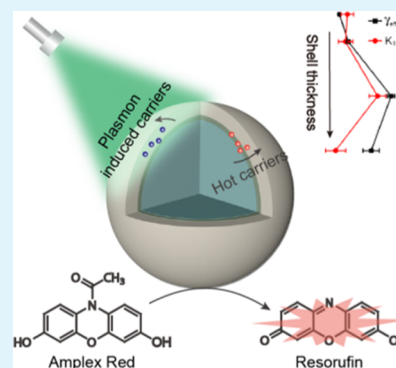
INTRODUCTION

Metal−semiconductor nanocatalysts (NCs) have attracted considerable attention in a wide range of fields from clean energy production, organic pollutant degradation to hazardous waste remediation.[1−3] Among those nanocomposites, noble-metal (e.g., gold and silver)-semiconductor (e.g., TiO$_2$) core−shell nanoparticles (NPs) are of particular interest because of their tunable optoelectronic properties and improved visible-light photocatalytic activity.[4−6] In metal−semiconductor heterojunctions, the metal surface plasmons are capable of inducing charge separation in semiconductors through plasmon-induced resonance energy transfer (PIRET) or a direct hot electron injection process.[7−9] Recent experimental and theoretical studies have led to progress in understanding how PIRET and hot electron transfer can independently enhance photocatalysis near or below the band edge of the semiconductor. However, investigation on how these two mechanisms coexist or compete in a plasmonic metal−semiconductor photocatalyst lags far behind. On the other hand, current studies on the relationship between the catalytic performance and the structural properties of the metal−semiconductor NCs have been mainly limited to only providing apparent averaged information at the ensemble level, which conceals the heterogeneous properties of individual NCs.[10−12] To get a deeper insight into the catalytic mechanism and the structure−activity relationship of the metal−semiconductor NCs, it is essential to study the catalytic process at the single-particle level.

Single-molecule fluorescence microscopy, with appealing features of multiplexed imaging, high sensitivity, and spatiotemporal resolution, allows in situ characterization of the catalytic kinetics and dynamics of individual NCs with single-turnover resolution.[13−15] To date, single-molecule fluorescence imaging has been exploited to resolve the heterogeneous NC structure-dependent reactivity, the dynamic evolution of catalytically active sites, and the activation energy by recording photo- and electro-catalytic transformations on different single isolated NCs, including semiconductors,[16−19] metal NPs,[20−23] and metal−semiconductor hybrids.[15,24] Recently, by incorporating competition into the single-molecule fluorescence detection scheme, non-fluorescent molecular conversions on single NCs have also recently been quantitatively imaged at the single-molecule level.[25] We envision that, by rationally designing the catalytic system, single-molecule fluorescence microscopy will enable the quantitative visualization of plasmon-enhanced photocatalytic transformation on single metal−semiconductor NCs and facilitate deciphering of the structure−function relationship.
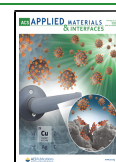
In this work, we report, to the best of our knowledge, the first direct characterization of metal−semiconductor NCs at the single-molecule and single-particle levels. As a proof-of-concept study, Ag@TiO$_2$ core−shell nanospheres with varied TiO$_2$ shell thickness were employed as model NCs. Ag@TiO$_2$ hybrid nanostructures are classical plasmonic metal−semiconductor NCs in which the generation and transport of charge carriers under photoexcitation may be complex depending on their structures.[6,26−28] By real-time recording of the fluorescence emission and measuring the reaction rate constant, we quantitatively demonstrate the heterogeneous catalytic dynamics of single NCs. The influence of TiO$_2$ shell thickness on the apparent catalytic activity was observed. Moreover, a mathematical model was established to resolve the contribution of PIRET-induced electron−hole (e$^-$/h$^+$) pairs and hot electrons that diffused to the outer surface of the TiO$_2$ shell in the catalytic reaction. Our single-molecule study enables a deeper understanding of the catalytic activity and the underlying mechanism of plasmonic metal−semiconductor NCs that should be useful not only for the design of new catalysts but also for the activity improvement of given NCs.

■ RESULTS AND DISCUSSION

The core−shell-structured NCs were synthesized by hydrolysis of titanium tetraisopropoxide (TTIP) on Ag NPs that were pre-coated with a thin layer of SiO$_2$ to decrease silver oxidation during TiO$_2$ deposition.[29,30] The transmission electron microscopy (TEM) measurements (Figures 1a,b and S1a,b)
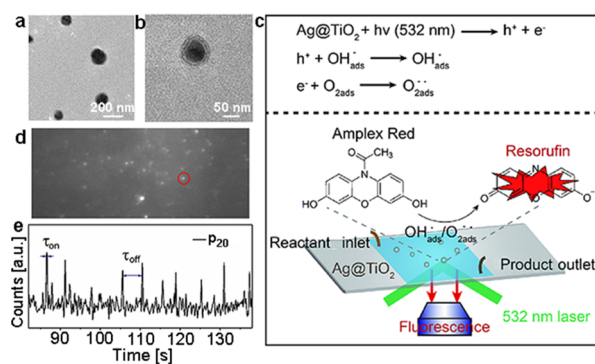

Figure 1. (a,b) Typical TEM image of p$_{20}$. (c) Top: Formation of radicals from the photogenerated e$^-$/h$^+$ of Ag@TiO$_2$ NCs. Bottom: TIRF microscopy to image the fluorescence reaction of Amplex Red illuminated by a 532 nm laser. (d) Fluorescence image of single-molecule nanocatalysts. (e) A segment of fluorescence trajectory from the spot marked by a red circle in d at 50 nM Amplex Red.

reveal that the Ag core has an average diameter of ca. 70 nm, which increases to ca. 110 nm after coating a 20 nm TiO$_2$ shell (denoted p$_{20}$ for simplicity). The energy-dispersive spectroscopy and X-ray diffraction analysis demonstrate the co-presence of Ag, Si, O, and Ti in core−shell NPs (Figure S1c−g). By adjusting the amount of TTIP, we prepared NCs with other thicknesses (5, 10, and 30 nm) of TiO$_2$ shells (denoted p$_5$, p$_{10}$, and p$_{30}$, respectively) (Figure S2). The UV−vis absorption spectrum of each hybrid NC shows a strong characteristic band at ca. 445 nm (Figure S3a) due to the localized surface plasmon resonance (LSPR) of the silver core and the effect of a thin SiO$_2$ interlayer.[29,31] Then, the plasmon peak gradually widens, accompanying the appearance and increase of a new absorption peak at ca. 320 nm (TiO$_2$, P25),

as the thickness of the TiO$_2$ layer increases from 5 to 30 nm. The experimental spectra are fully consistent with the results predicted by Mie theory calculations (Figure S3b). Both the experimental and theoretical studies demonstrate that the semiconductor shell negligibly affects the absorption of the hybrid NC to light as the wavelength is increased beyond 400 nm (Figure S3). To further verify this, the absorption spectra of 70 nm Ag NPs and 25 nm TiO$_2$ NPs were determined. As shown in Figure S4, TiO$_2$ NPs have a single sharp peak at ca. 320 nm that rapidly decays to near zero at ca. 400 nm. Since we use a 532 nm laser to induce the catalytic reaction, the TiO$_2$ layer is therefore considered light-transparent to the excitation light. That is, the TiO$_2$ shell itself has no interaction with the laser excitation during the photocatalytic process, which is important to clarify the catalytic mechanism in later sections.

As depicted in Figure 1c, the single-molecule imaging of photocatalytic reaction is based on a total internal reflection fluorescence (TIRF) microscopy of a fluorogenic catalytic reaction. Ag@TiO$_2$ NCs can be excited with a 532 nm laser to generate e$^-$/h$^+$ pairs in the semiconductor shell. The photoinduced charge carriers produce adsorbed hydroxyl radicals (OH$^·_{ads}$) and superoxide anion radicals (O$^{-·}_{ads}$) on the NC surface, respectively, by further reaction with H$_2$O$_{ads}$/OH$^-_{ads}$ or O$_{2ads}$. The absorbed radicals then oxidize Amplex Red, a non-fluorescent compound, to its highly fluorescent product Resorufin,[32] which is observed using a high-numerical aperture oil immersion objective and imaged with a sensitive electron-multiplying charge-coupled device (EM-CCD) camera. A micro-flow cell was used to supply a continuous and constant flow of the reactant Amplex Red solution to the NC surface (Figure S5). Before single-molecule measurements, the feasibility of the reaction system was initially validated by the ensemble experiments (Figure 3). The photocatalytic reactions were first carried out in PBS buffer containing 10 μM Amplex Red and 0.1 mg/mL Ag@TiO$_2$ NCs and excited by a 532 nm laser for different times. From Figure 3a−b, one can see that no product molecules were formed in the solution without light illumination. After illuminated with 532 nm light for 20 min, a new absorption peak at about 570 nm and a fluorescence emission peak at about 585 nm appeared, implying that Resorufin was generated from the reaction of Amplex Red catalyzed by NCs. When increasing the illumination time, the fluorescence intensity increased gradually, indicating that more product molecules were generated on the catalyst surface (Figure 3b,c). In addition, a new molecule with m/z of 214.55 in the mass spectra was generated after the reaction, which was highly consistent with the molecular weight of Resorufin (Figure 3d). With up to 100 ms frame rate, we recorded movies of stochastic fluorescent bursts at a localized spot on the glass surface (Figure 1d). Figures 1e and S6a display the typical time trajectories of fluorescence intensity from a single-molecule catalytic movie, each sharp intensity spike marking the formation of Resorufin on the NC surface; the falling of fluorescence intensity spike to the baseline level marks a short dissociation of the product molecules from the particle surface (Figure S7), and each off−on corresponds to a single turnover of catalytic formation of a product on one NC and its subsequent dissociation. Control experiments show that no clear fluorescent bursts are observed in the absence of substrate, and no clear fluorescent bursts are observed on pure Ag@SiO$_2$ or TiO$_2$ NPs (Figure S8). Thus,
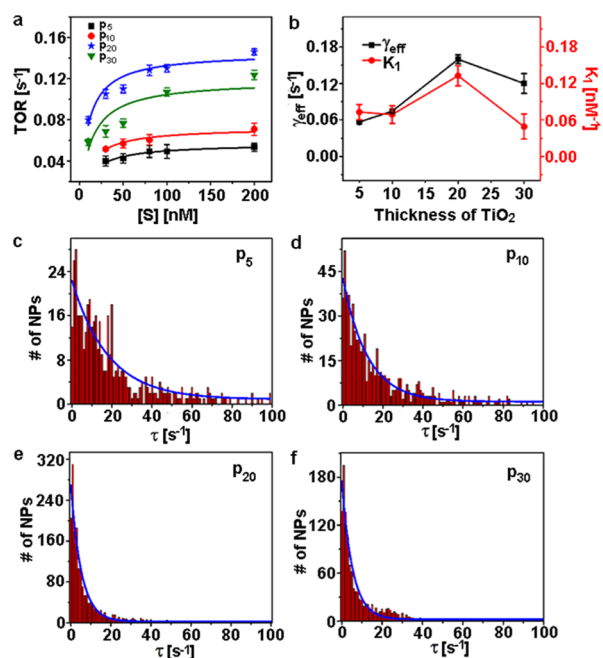
Figure 2. (a) Amplex Red concentration dependence of TOR with different NPs as the catalyst. Each data point is an average of more than 50 individual NCs. Error bars are standard errors of mean. (b) γ_{eff} and K_1 vs different NCs. Error bars are standard deviations. Distributions of τ_{off} (c, p$_5$), (d, p$_{10}$), (e, p$_{20}$), and (f, p$_{30}$) from more than 50 trajectories at 100 nM Amplex Red.

bursts on the trajectories indicate that the new product molecules dissociate very fast after their formation on a NP surface. Thus, the τ_{on} can be neglected and τ_{off} can be approximately regarded as the time needed to complete a catalytic turnover.[32] Then, the average turnover rate (TOR) of a single NP can be derived directly by counting the number of bursts within a given time with TOR = $\langle \tau_{off} \rangle^{-1}$, where $\langle \rangle$ denotes averaging. To probe the kinetic mechanism of NCs with different TiO$_2$ shell thicknesses, we investigated their activities by conducting catalytic turnovers with different concentrations of Amplex Red [S]. The [S] concentration titration curves of TOR for different NCs are displayed in Figure 2a, and each curve is averaged over many NCs. Apparently, the TORs increased with increasing substrate concentration and then reaches saturation but with different saturation levels and initial slopes, reflecting their hetero-geneity in catalytic reactivity. The dependence of TOR on [S] can be described by the Langmuir−Hinshelwood equation[32]

$$\text{TOR} = \langle \tau_{off} + \tau_{on} \rangle^{-1} \approx \langle \tau_{off} \rangle^{-1} = \frac{\gamma_{eff} K_1 [S]}{1 + K_1 [S]} \qquad (1)$$

where γ_{eff} is the effective catalytic rate constant, representing the reactivity of NCs and K_1 is the equilibrium adsorption constant of the substrate on NCs. By fitting the data with eq 1, and as shown in Figure 2a, the values of γ_{eff} and K_1 for the catalysis with different NCs are displayed in Table 1. The

Table 1. Results of the Fits to eqs 1 and 2 for the Reactions on Different NCs

catalysts	γ_{eff} [s^{-1}][a]	K_1 [nM^{-1}][b]	γ_{app} [s^{-1}][c]
p$_5$	0.057 ± 0.002	0.073 ± 0.013	0.055 ± 0.075
p$_{10}$	0.072 ± 0.003	0.069 ± 0.014	0.081 ± 0.005
p$_{20}$	0.15 ± 0.01	0.13 ± 0.02	0.19 ± 0.01
p$_{30}$	0.12 ± 0.01	0.052 ± 0.025	0.14 ± 0.03

[a]Net reactivity of individual NCs. [b]Equilibrium adsorption constant. [c]Formation rate constant of Resorufin.

kinetic parameters derived from these four NCs give an insight into the kinetics: (1) p$_{20}$ possesses the largest value of γ_{eff} and K_1, suggesting that a 20 nm thickness of TiO$_2$ has higher activity in the catalytic product formation reaction. (2) Originally, the values of γ_{eff} and K_1 show a clear increasing trend as the semiconductor layer thickness increases from 5 to 20 nm. This trend is due to the increase in the number of e$^-$/h$^+$ pairs as the film thickness increases, resulting in the increased probability of the catalytic collision. (3) A further increase in the shell thickness diminishes the values of γ_{eff} and K_1. This is because the diffusion length of energetic carriers increases as the film thickness increases, resulting in the attenuation of plasma enhancement and reduction in the efficiency of catalytic reactions. Figure 2b displays the point-plot of γ_{eff} and K_1 versus the thickness of TiO$_2$, which clearly indicates the trend between the shell thickness and the values of γ_{eff} and K_1. Control experiments show that there is no obvious TOR difference between different laser powers and no clear visible difference in TOR upon repeating the same experiment under the exactly same conditions, indicating that the fluorescent bursts are not photo-induced and the system and results are stable (Figure S9).

The catalytic activity of different NCs was also quantified by plotting the distribution of τ_{off} from many NC turnover
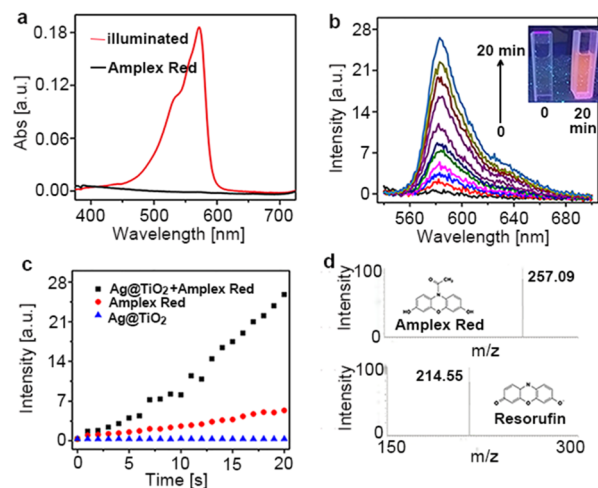

Figure 3. (a) UV−vis absorption spectra and (b) fluorescence spectra of Amplex Red and p$_{20}$ in PBS before and after illumination with a laser for 20 min. Inset in b shows the fluorescence photos of Amplex Red before and after illumination for 20 min. (c) Fluorescence intensity at 585 nm versus time data after the laser light is turned on. (d) Mass spectra of Amplex Red before and after illumination for 20 min.

the single-Resorufin fluorescent burst is attributed to the single catalytic turnover by a single Ag@TiO$_2$ particle.

In the single-molecule fluorescence trajectories (Figures 1e and S6a), the time interval (τ_{off}) of two adjacent bursts is the waiting time before the formation of a fluorescent product molecule; the values of τ_{off} are stochastic, and their distributions can reflect the underlying catalytic reaction kinetics. τ_{on} is the standing time before the product molecules dissociated from the surface of NCs. Notably, the narrow

trajectories. The probability density functions of τ_{off} and $f(\tau_{off})$ can be evaluated by eq 2[32]

$$f_{off}(\tau) = \gamma_{app} \exp(-\gamma_{app}\tau) \qquad (2)$$

Here, γ_{app} is the averaged apparent formation rate constant of Resorufin on the surface of many NCs. Figure 2c−f shows the typical histogram distributions of τ_{off} from the four types of NCs. The solid curves are the fitting results based on eq 2 to obtain γ_{app}. As shown in Table 1, the γ_{app} value of p_{20} is larger than that of others, indicating that the production formation on p_{20} is the fastest and p_{20} possesses the highest intrinsic catalytic activity, which is consistent with the above results related to γ_{eff} shown in Table 1.

The nanoscale catalysts are usually unstable and can restructure dynamically, where the dynamic surface restructuring can be further induced by the constantly fluctuating adsorbate−surface interactions. The temporal variation frequency of catalytic turnovers from a single-turnover trajectory can be used to evaluate the underlying dynamic activity fluctuations of single NCs. Currently, the temporal activity fluctuations of single NCs have been demonstrated at the single-molecule level, and it is considered that such activity fluctuations come from the spontaneous surface atom recombination or catalytic reaction. Here, we extracted the sequence of individual τ from the turnover trajectory and then calculated their autocorrelation function $C_\tau(m) = \langle\Delta\tau(0)\Delta\tau(m)\rangle/\langle\Delta\tau^2\rangle$,[32] where τ is τ_{off}, m is the catalytic turnover index number in the sequence, and $\Delta\tau(m) = \tau(m) - \langle\tau\rangle$. In the presence of catalytic activity fluctuations, $C_\tau(m)$ shows a decay behavior with the decay time constant, suggesting the underlying fluctuation correlation time.[33,34] For a single NC with different TiO_2 shell thicknesses, Figure 4 shows that $C_\tau(m)$ exhibits a single-exponential decay behavior, directly indicating the temporal catalytic activity fluctuations of the NCs. The exponential decay constants of $C_\tau(m)$ are 1.8 ± 0.3 turnovers for the individual p_{20}, and 7.8 ± 2.2, 4.1 ± 1.5, and 4.5 ± 1.3 turnovers for the individual p_5, p_{10}, and p_{30},

respectively. $C_\tau(m)$ of each NC can then be converted to $C_\tau(t)$ in which the turnover index m is converted to real time t using the average turnover time of a single NC. When $C_\tau(t)$ is averaged over many NCs, their exponential decay behavior is preserved (Figure 4 inset). The corresponding decay time constants are 124 ± 34, 80 ± 25, 25 ± 6, and 82 ± 29 s, respectively, which are the activity fluctuation time scales and also reflect the times scales of the underlying dynamic surface restructuring at the respective active sites on the NCs. The values revealed the underlying dynamic surface restructuring rates of single NCs during the catalytic process.

To understand the observation of the maximum catalytic efficiency at 20 nm TiO_2 shell thickness, we built a computational model to quantitatively describe the mechanism of photoinduced catalysis that occurred on such plasmonic metal−semiconductor NCs. The model assumes that the reactive probability of a single NC is proportional to the total electron number of free radicals generated on the TiO_2 shell surface, which is dependent on the actual number of energetic electrons if we do not consider the contribution of holes for now. The surface electrons comprise two parts: (1) N_1, the electrons of e^-/h^+ pairs excited around the TiO_2 surface by the PIRET effect[36,37] and (2) N_2, the hot electrons that are generated on the Ag core by LSPR and injected into the TiO_2 shell and diffused to its outer surface. Considering these two aspects, we described the catalytic probability P as follows

$$P \propto N_{tot} = N_1 + N_2 \qquad (3)$$

where N_1 is the e^-/h^+ pair density near the TiO_2 surface, which is calculated by the integration of laser E-intensity within the surface area (eq S1), and N_2 is the hot electron number on the TiO_2 surface, which is obtained by solving the differential diffusion equations at the spherical coordinate (eqs S2−S4). Thus, the catalytic probability can be finally expressed aswhere α_1 is the photo-electron conversion efficiency of TiO_2, λ_{pe} is the mean free path of photo-electrons beyond which the e^-/h^+ pairs in the TiO_2 are assumed to recombine and not contribute to the catalysis, $R_0 = r_0+d_{in} + d$ is the outer radius of the nanocrystal that equals the Ag core radius r_0 plus SiO_2 thickness d_{in} and TiO_2 thickness d, ρ is the conversion coefficient of hot electrons, β_2 is the tunneling efficiency, D_{dif} is the diffusion coefficient, and $erfc(x)$ is the Gauss error function obtained from solving the diffusion equation.

It is worth pointing out that the calculation of catalytic probability pre-requires the calculation of the enhanced E-field distribution in the nanocrystal. We calculated the intensity distribution of E-field on the Ag core surface. The E-field intensity is axis-symmetrically distributed along the light-beam propagation direction. The E-field intensity rises gradually from zero at two poles and reaches the maximum at the equator circle. Along the radius direction, the intensity is quite stronger outside the metal core than on the inside. The E-field distributions in Figure 5c−f show the enhancement effect of LSPR clearly, and it also reveals the collective electron resonant nature of LSPR. Remarkably, the intensity of E-field on the TiO_2 layer outer surface shows a clear incline with respect to the increase of TiO_2 shell thickness, as shown in Figure 5a.

Once we calculated the E-field distribution in the surrounding space of the NC particle with varying TiO_2 shell thicknesses, we can calculate the photo-electron term and the hot electron term based on N_1 and N_2 (eqs S1−S4). It is worth pointing out that both terms are the product of the integration
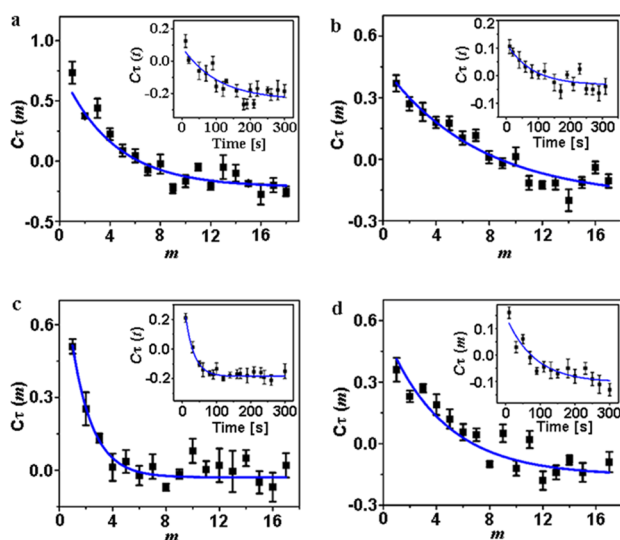

Figure 4. Autocorrelation function $C_\tau(m)$ of m from the catalytic turnover trajectory of a single (a) p_5, (b) p_{10}, (c) p_{20}, and (d) p_{30} NC at 100 nM Amplex Red. Inset: autocorrelation function $C_\tau(t)$ of τ from the fluorescence turnover trajectories of single NCs. Solid line is the single-exponential equation fitting.
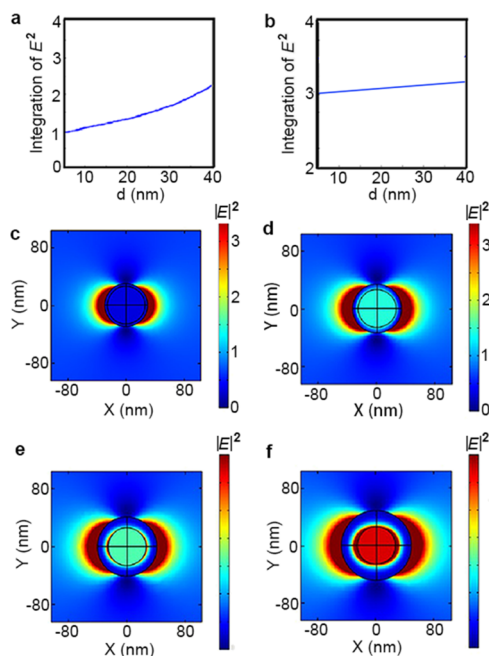
Figure 5. (a) Integration of $|E|^2$ in the NC outer layer surface that determines the photo-electron contribution to the catalysis activity. (b) Integration of $|E|^2$ on the Ag core surface that determines the contribution of hot electrons to the catalytic activity. The electromagnetic field enhancement $|E|^2$ for (c) p_5, (d) p_{10}, (e) p_{20}, and (f) p_{30} NCs.

of $|E|^2$ and the combination of some materials parameters such as α_1, ρ, β_2, and D_{dif}. Most of these material parameters are independent of TiO_2 shell thickness d, while D_{dif} varies slightly with d. The parts of $|E|^2$ integration in two terms show different trends vs d, as shown in Figure 5a,b. The joint contribution to the catalytic probability by the photo-electron term and the hot electron term that have mono inclining and declining trends, respectively, results in the existence of an optimal TiO_2 thickness d generating the maximal catalytic probability. Obviously, the exact value of the optimal d is determined by the relative weight of the N_1 and N_2 terms in eqs 3 or 4.

$$P(d) \propto \alpha_1 \lambda_{pe} \iint \left| E(r|r=R_0) \right|^2 dS + \beta_2 \rho \lambda_{he} \frac{r_0 + d}{r_0} erfc\left(\frac{d}{2\sqrt{D_{dif}}}\right) \iint \left| E(r|r=r_0) \right|^2 dS \quad (4)$$

However, β_2 is difficult to measure or calculate because the SiO_2 layer of the nanocrystal is not a lattice structure, and the energy-band theory calculation would encounter significant uncertainty. The similar issue happens in the determination of ρ and D_{dif} of the TiO_2 shell. Relatively, the assumption that the ρ equals its corresponding bulk value is slightly more reliable, but the validation of such assumption is also under question since the structure of the metal core may be different from the common bulk Ag. In order to deal with the uncertainty of material parameters, we rewrite the catalysis efficiency in eq 4 into a new form as

$$P(d) \propto I_1 + c_{21}I_2 \quad (5)$$

Similarly, we convert several parameters into one apparent weight factor that determines the relative contribution of E-field integration on the Ag core surface and that on the TiO_2 layer surface to the catalytic activity of the NCs (eqs S5−S7).

In order to study the effect of layer thickness, we can split the weight factor c_{21} into two factors

$$c_{21} = c_m \cdot c_g \quad (6)$$

where

$$c_g = \frac{r_0 + d}{r_0} erfc\left(\frac{d}{2\sqrt{D_{dif}}}\right) \quad (7)$$

and

$$c_m = \frac{\beta_2 \rho \lambda_{he}}{\alpha_1 \lambda_{te}} \quad (8)$$

refer to the geometry factor and material factor, respectively. The former one is dependent on the TiO_2 thickness d and the latter one is not. Using the initial diffusion coefficient $D_0 \sim 700$ nm^2/s and the diffusion time constant $\tau \sim 0.06$ s,[35] c_g versus d is plotted in Figure 6a−c. A key feature of such plots is that
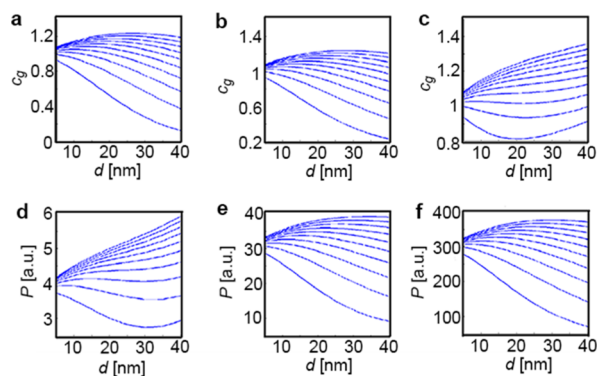

Figure 6. (a) Plot dependence of geometry factor c_g on the shell thickness with varying diffusion times τ (a, $\tau = 0.01$), (b, $\tau = 0.06$), and (c, $\tau = 0.1$). The catalytic probability P vs d with a specific diffusion time ($\tau = 0.06$) and varying material factor c_m (d, $c_m = 1$), (e, $c_m = 10$), and (f, $c_m = 100$).

under certain parameters of D_0 and τ, the c_g rises to a maximum and then declines versus d. While the c_m and E-field integrations I_1 and I_2 are either independent of or ascends against d, c_g declines in a certain range of d and causes the rising and then the falling trend of catalytic activity versus d that was observed experimentally, as shown in Figure 2b.

Furthermore, we calculated the effect of c_m on the diffusion time $\tau = 0.06$ s, which is the experimental value obtained from the literature.[35] The calculated curve of catalysis efficiency clearly shows that the optimal thickness d shifts from a small value to the larger ones when the c_m becomes larger, which means that the contribution of hot electrons increases relatively largely (Figure 6d−f). Taken together, the above analysis indicates that the photogenerated electrons and the hot electrons simultaneously participate in the catalytic process, and the contribution of the two aspects to the catalytic efficiency depends on the structure (e.g., TiO_2 thickness) of the catalytic NPs.

■ CONCLUSIONS

In this work, the transient and quantitative in situ single-molecule study of the semiconductor thickness effect on plasmon-enhanced photocatalytic redox at single Ag@TiO_2 core−shell NC levels has been demonstrated. Both the

effective catalytic rate constant of individual NCs and the apparent formation rate constant of the reaction products are found to increase first and then decrease with increasing thickness of the TiO_2 nanoshell. Furthermore, the dynamic fluctuation of the catalytic activity during continuous redox conversion is also quantitatively characterized by resolving the self-correlated function. On the basis of the Langmuir—Hinshelwood mechanism, we find that the four NCs studied in the present work exhibit different adsorption and oxidation abilities to the reactant molecules. Moreover, a mathematical model was first developed to explain the underlying mechanism of catalysis by considering the two types of carrier contributions from the photoelectron generation in the TiO_2 semiconductor shell and hot electrons generated at the Ag core surface. Briefly, the former contribution increases with expanding thickness of the TiO_2 shell from 5 to 30 nm because both the E-field intensity and outer surface area increase monotonically in this thickness scale. However, the contribution of hot electrons is affected by the diffusion process in the semiconductor shell whose thickness causes loss and the arriving-surface delay of hot electrons. Such a negative effect of hot electron diffusion counteracts the positive effect of TiO_2 thickness on the E-field enhancement, as well as the inclining trend of the contribution of photo-electrons, that results in the maximal catalytic activity at 20 nm TiO_2 thickness. The mechanism insight obtained by our single-molecule analysis is complementary to the previous ensemble experiment and can promote an understanding of the structure—performance relationship of other metal—semi-conductor hybrid NCs. In the future, it is necessary to improve the reaction system to study the contribution of heat and energetic charge carriers in specific photocatalytic reactions, which is very important for the design of new plasma NCs.[38,39]

MATERIALS AND METHODS

Synthesis of Ag@TiO_2 NCs. Ag@TiO_2 core—shell NCs were synthesized by a three-step procedure.[29,30] For synthesis of the silver core, $AgNO_3$ (0.38 g) and PVP (2.5 g) in 150 mL of ethylene glycol were heated to 130 °C in 20 min under vigorous stirring. The reaction solution was incubated for 1 h at 130 °C without further stirring and then Ag NPs were precipitated by the addition of 500 mL of acetone. The synthesized Ag NPs were washed twice using ethanol and water and redispersed in ethanol for further use. To form an ultrathin interlayer (~2 nm thickness) of silica on the outer surface of Ag NPs, the purified Ag colloids were dissolved in 140 mL of ethanol and stirred for 30 min at room temperature and then 30 mL of water and 1.8 mL of $NH_3 \cdot H_2O$ were added to the mixture under stirring. Afterward, 23 μL of tetraethyl orthosilicate dissolved in 14 mL of ethanol was added dropwise into the suspension, followed by continuously stirring for 12 h. The as-prepared Ag@SiO_2 NPs were washed with ethanol and water and redispersed in 90 mL of ethanol. To functionalize the Ag@SiO_2 NPs with amino groups, the NP solution was mixed with 150 μL of APTMS, followed by refluxing at 85 °C for 4 h. The NPs were cleaned by centrifugation and dispersed in 10 mL of ethanol. To form a layer of TiO_2 on the outer surface of Ag@SiO_2 NPs, 10 mL of amine-modified Ag@SiO_2 NPs were dispersed in 150 mL of ethanol and stirred for 3 h at room temperature; 150 μL of TTIP ethanol solution previously dissolved in 30 mL of ethanol was then added dropwise to the NP dispersion under stirring, followed by refluxing at 80 °C for 2 h. The sediments were centrifuged, washed with water, dried at 60 °C, and calcined at 450 °C in air for 2 h to remove the organic species and improve the crystallinity. The thickness of the formed TiO_2 shell was about 20 nm. For simplicity, this nanoparticle was named p_{20}. To prepare Ag@TiO_2 NPs with other thickness TiO_2 shells, the volume of TTIP (50 μL,

100 μL, and 300 μL) was varied, while keeping all other procedures unchanged, and the corresponding NPs were named p_5, p_{10}, and p_{30}, respectively.

Sample Preparation. Coverslips were first washed by sequential sonication in 1 M KOH, Milli-Q water, ethanol, and Milli-Q water, each for 10 min. Then, the slides were dried under a N_2 stream. To prepare the Ag@TiO_2 NC-coated coverslip, a slurry was first prepared by sonicating 5 mg of NCs in 1 mL of water for 30 min. 20 μL of diluted slurry was then adsorbed onto the surface of coverslip for 10 min and washed with 50 mM PBS (pH 7.3) to remove the excess particles. A flow cell (height × length × width = 100 μm × 2 cm × 5 mm) was formed using a double-sided tape as an intermediary to seal up the space between the quartz slide and the coverslip, then the outer edges of the tape were sealed by 5 min-epoxy (Devcon, USA). On the quartz slide, two holes (diameter ~ 1 mm) were drilled to connect to the polyethylene tubing and the syringe pump for continuous solution flow at 20 μL/min (Figure S5).

Single-Molecule Fluorescence Measurements. Single-molecule fluorescence measurements were performed on a home-built prism-type TIRF microscope based on an Olympus IX 73 inverted microscope. The 532 nm laser beam was focused by a wide-field lens and applied to directly excite both the Ag@TiO_2 NCs and the fluorescence of Resorufin. The fluorescence of Resorufin was collected using a 100× NA1.45 oil-immersion objective (Optosplit II, Andor Technology Plc., U.K.), filtered using a filter (HQ545LP), and projected onto an EM-CCD camera (iXon DU897, Andor Technology Plc., U.K.) operated at a frame rate of 100 ms. In the experiments, the fluorescent dust or impurities in the flow channel were first photobleached by flowing in PBS and shining a high-power density green laser for 30 min. In this way, most of the fluorescent impurities could be photobleached and the remaining dusts with stable fluorescence were used as markers. After that, buffers containing different concentrations of Amplex Red were flowed through the flow cell and illuminated with a laser at an appropriate intensity. The movies were analyzed using a home-written MATLAB program, which extracted the fluorescence intensity trajectories from localized fluorescence spots individually across the entire movie (Figures 1d,e and S6a). The data analysis process is shown in Section 2 of the Supporting Information.

ASSOCIATED CONTENT

ⓈⒾ Supporting Information

The Supporting Information is available free of charge at https://pubs.acs.org/doi/10.1021/acsami.0c18508.

> Materials; data analysis process; key points on how to get clean or real single-molecule photocatalytic signals; more details about the calculation results; character-ization of NCs; setup of the flow cell; and control experiments (PDF)

AUTHOR INFORMATION

Corresponding Authors

Lei Zhou — *Department of Physics, Fudan University, Shanghai 200433, China*; Email: phzhou@fudan.edu.cn

Jianwei Liu — *Department of Chemistry, Shanghai Stomatological Hospital, State Key Laboratory of Molecular Engineering of Polymers, Fudan University, Shanghai 200433, China*; Email: jianweiliu@fudan.edu.cn

Baohong Liu — *Department of Chemistry, Shanghai Stomatological Hospital, State Key Laboratory of Molecular Engineering of Polymers, Fudan University, Shanghai 200433, China*; ⓞ orcid.org/0000-0002-0660-8610; Email: bhliu@fudan.edu.cn

Authors

Yujie Liu − *Department of Chemistry, Shanghai Stomatological Hospital, State Key Laboratory of Molecular Engineering of Polymers, Fudan University, Shanghai 200433, China*

Kun Zhang − *Department of Chemistry, Shanghai Stomatological Hospital, State Key Laboratory of Molecular Engineering of Polymers, Fudan University, Shanghai 200433, China*

Xiaochaoran Tian − *Department of Physics, Fudan University, Shanghai 200433, China*

Complete contact information is available at:
https://pubs.acs.org/10.1021/acsami.0c18508

Author Contributions

Y.L., K.Z., and X.T. contributed equally to this work. J.L. and B.L. conceived the original concept and supervised the project. Y.L. and K.Z. prepared the materials and performed the experiments. X.T., L.Z., and J.L. conducted the simulations and calculations. Y.L., K.Z., J.L., X.T., L.Z., and B.L. analyzed the data and wrote the paper. All authors discussed the results and commented on the manuscript.

Notes

The authors declare no competing financial interest.

■ REFERENCES

(1) Linic, S.; Christopher, P.; Ingram, D. B. Plasmonic-Metal Nanostructures for Efficient Conversion of Solar to Chemical Energy. *Nat. Mater.* **2011**, *10*, 911−921.

(2) Jiang, R.; Li, B.; Fang, C.; Wang, J. Metal/Semiconductor Hybrid Nanostructures for Plasmon-Enhanced Applications. *Adv. Mater.* **2014**, *26*, 5274−5309.

(3) Liu, X.; Iocozzia, J.; Wang, Y.; Cui, X.; Chen, Y.; Zhao, S.; Li, Z.; Lin, Z. Noble Metal-Metal Oxide Nanohybrids with Tailored Nanostructures for Efficient Solar Energy Conversion, Photocatalysis and Environmental Remediation. *Energy Environ. Sci.* **2017**, *10*, 402−434.

(4) Teranishi, M.; Hoshino, R.; Naya, S.-i.; Tada, H. Gold-Nanoparticle-Loaded Carbonate-Modified Titanium(IV) Oxide Surface: Visible-Light-Driven Formation of Hydrogen Peroxide from Oxygen. *Angew. Chem., Int. Ed.* **2016**, *55*, 12773−12777.

(5) Li, W.; Elzatahry, A.; Aldhayan, D.; Zhao, D. Core-Shell Structured Titanium Dioxide Nanomaterials for Solar Energy Utilization. *Chem. Soc. Rev.* **2018**, *47*, 8203−8237.

(6) Hong, D.; Lyu, L.-M.; Koga, K.; Shimoyama, Y.; Kon, Y. Plasmonic Ag@TiO2 Core-Shell Nanoparticles for Enhanced CO2 Photoconversion to CH4. *ACS Sustainable Chem. Eng.* **2019**, *7*, 18955−18964.

(7) Knauf, R. R.; Kalanyan, B.; Parsons, G. N.; Dempsey, J. L. Charge Recombination Dynamics in Sensitized SnO2/TiO2 Core/Shell Photoanodes. *J. Phys. Chem. C* **2015**, *119*, 28353−28360.

(8) Forato, F.; Talebzadeh, S.; Bujoli, B.; Queffélec, C.; Trammell, S. A.; Knight, D. A. Core-Shell Ag@TiO2Nanocomposites for Low-Power Blue Laser Enhanced Copper(I) Catalyzed Ullmann Coupling. *ChemistrySelect* **2017**, *2*, 769−773.

(9) Parente, M.; Sheikholeslami, S.; Naik, G. V.; Dionne, J. A.; Baldi, A. Equilibration of Photogenerated Charge Carriers in Plasmonic Core@Shell Nanoparticles. *J. Phys. Chem. C* **2018**, *122*, 23631−23638.

(10) Collado, L.; Reynal, A.; Fresno, F.; Barawi, M.; Escudero, C.; Perez-Dieste, V.; Coronado, J. M.; Serrano, D. P.; Durrant, J. R.; de la Peña O'Shea, V. A. Unravelling the Effect of Charge Dynamics at the Plasmonic Metal/Semiconductor Interface for CO2 Photoreduction. *Nat. Commun.* **2018**, *9*, 4986.

(11) He, S.; Huang, J.; Goodsell, J. L.; Angerhofer, A.; Wei, W. D. Plasmonic Nickel-TiO 2 Heterostructures for Visible-Light-Driven Photochemical Reactions. *Angew. Chem., Int. Ed.* **2019**, *58*, 6038−6041.

(12) Du, L.; Shi, G.; Zhao, Y.; Chen, X.; Sun, H.; Liu, F.; Cheng, F.; Xie, W. Plasmon-Promoted Electrocatalytic Water Splitting on Metal-Semiconductor Nanocomposites: the Interfacial Charge Transfer and the Real Catalytic Sites. *Chem. Sci.* **2019**, *10*, 9605−9612.

(13) Zou, N.; Zhou, X.; Chen, G.; Andoy, N. M.; Jung, W.; Liu, G.; Chen, P. Cooperative communication within and between single nanocatalysts. *Nat. Chem.* **2018**, *10*, 607−614.

(14) Zhou, J.; Chizhik, A. I.; Chu, S.; Jin, D. Single-Particle Spectroscopy for Functional Nanomaterials. *Nature* **2020**, *579*, 41−50.

(15) Dong, B.; Pei, Y.; Zhao, F.; Goh, T. W.; Qi, Z.; Xiao, C.; Chen, K.; Huang, W.; Fang, N. In Situ Quantitative Single-Molecule Study of Dynamic Catalytic Processes in Nanoconfinement. *Nat. Catal.* **2018**, *1*, 135−140.

(16) Sambur, J. B.; Shepherd, D. P.; Hesari, M.; Van Erdewyk, M.; Choudhary, E.; Chen, P. Correlated Single-Molecule Reaction Imaging and Photocurrent Measurements Reveal Underlying Rate Processes in Photoelectrochemical Water Splitting. *J. Electrochem. Soc.* **2019**, *166*, H3286−H3293.

(17) Hesari, M.; Sambur, J. B.; Mao, X.; Jung, W.; Chen, P. Quantifying Photocurrent Loss of a Single Particle-Particle Interface in Nanostructured Photoelectrodes. *Nano Lett.* **2019**, *19*, 958−962.

(18) Hesari, M.; Mao, X.; Chen, P. Charge Carrier Activity on Single-Particle Photo(electro)catalysts: Toward Function in Solar Energy Conversion. *J. Am. Chem. Soc.* **2018**, *140*, 6729−6740.

(19) Sambur, J. B.; Chen, T.-Y.; Choudhary, E.; Chen, G.; Nissen, E. J.; Thomas, E. M.; Zou, N.; Chen, P. Sub-Particle Reaction and Photocurrent Mapping to Optimize Catalyst-Modified Photoanodes. *Nature* **2016**, *530*, 77−80.

(20) Li, W.; Miao, J.; Peng, T.; Lv, H.; Wang, J.-G.; Li, K.; Zhu, Y.; Li, D. Single-Molecular Catalysis Identifying Activation Energy of the Intermediate Product and Rate-Limiting Step in Plasmonic Photocatalysis. *Nano Lett.* **2020**, *20*, 2507−2513.

(21) Zou, N.; Chen, G.; Mao, X.; Shen, H.; Choudhary, E.; Zhou, X.; Chen, P. Imaging Catalytic Hotspots on Single Plasmonic Nanostructures via Correlated Super-Resolution and Electron Microscopy. *ACS Nano* **2018**, *12*, 5570−5579.

(22) Chen, G.; Zou, N.; Chen, B.; Sambur, J. B.; Choudhary, E.; Chen, P. Bimetallic Effect of Single Nanocatalysts Visualized by Super-Resolution Catalysis Imaging. *ACS Cent. Sci.* **2017**, *3*, 1189−1197.

(23) Zhang, Y.; Chen, T.; Alia, S.; Pivovar, B. S.; Xu, W. Single-Molecule Nanocatalysis Shows in Situ Deactivation of Pt/C Electrocatalysts During the Hydrogen-Oxidation Reaction. *Angew. Chem., Int. Ed.* **2016**, *55*, 3086−3090.

(24) Huang, X.; Li, H.; Zhang, C.; Tan, S.; Chen, Z.; Chen, L.; Lu, Z.; Wang, X.; Xiao, M. Efficient Plasmon-Hot Electron Conversion in Ag-CsPbBr3 Hybrid Nanocrystals. *Nat. Commun.* **2019**, *10*, 1163.

(25) Mao, X.; Liu, C.; Hesari, M.; Zou, N.; Chen, P. Super-resolution imaging of non-fluorescent reactions via competition. *Nat. Chem.* **2019**, *11*, 687−694.

(26) Hirakawa, T.; Kamat, P. V. Photoinduced Electron Storage and Surface Plasmon Modulation in Ag@TiO2Clusters. *Langmuir* **2004**, *20*, 5645−5647.

(27) Lee, H.; Lee, Y. K.; Hwang, E.; Park, J. Y. Enhanced Surface Plasmon Effect of Ag/TiO2 Nanodiodes on Internal Photoemission. *J. Phys. Chem. C* **2014**, *118*, 5650−5656.

(28) Awazu, K.; Fujimaki, M.; Rockstuhl, C.; Tominaga, J.; Murakami, H.; Ohki, Y.; Yoshida, N.; Watanabe, T. A Plasmonic Photocatalyst Consisting of Silver Nanoparticles Embedded in Titanium Dioxide. *J. Am. Chem. Soc.* **2008**, *130*, 1676−1680.

(29) Zhang, X.; Zhu, Y.; Yang, X.; Wang, S.; Shen, J.; Lin, B.; Li, C. Enhanced Visible Light Photocatalytic Activity of Interlayer-Isolated Triplex Ag@SiO$_2$@TiO$_2$ Core-Shell Nanoparticles. *Nanoscale* **2013**, *5*, 3359−3366.

(30) Yang, J.; Zhang, F.; Chen, Y.; Qian, S.; Hu, P.; Li, W.; Deng, Y.; Fang, Y.; Han, L.; Luqman, M.; Zhao, D. Core-Shell Ag@SiO$_2$@mSiO$_2$ Mesoporous Nanocarriers for Metal-Enhanced Fluorescence. *Chem. Commun.* **2011**, *47*, 11618−11620.

(31) Kumar, M. K.; Krishnamoorthy, S.; Tan, L. K.; Chiam, S. Y.; Tripathy, S.; Gao, H. Field Effects in Plasmonic Photocatalyst by Precise SiO$_2$ Thickness Control Using Atomic Layer Deposition. *ACS Catal.* **2011**, *1*, 300−308.

(32) Xu, W.; Kong, J. S.; Yeh, Y.-T. E.; Chen, P. Single-Molecule Nanocatalysis Reveals Heterogeneous Reaction Pathways and Catalytic Dynamics. *Nat. Mater.* **2008**, *7*, 992−996.

(33) Lu, H. P.; Xun, L.; Xie, X. S. Single-Molecule Enzymatic Dynamics. *Science* **1998**, *282*, 1877−1882.

(34) Witkoskie, J. B.; Cao, J. Single Molecule Kinetics. I. Theoretical Analysis of Indicators. *J. Chem. Phys.* **2004**, *121*, 6361−6372.

(35) Nakade, S.; Saito, Y.; Kubo, W.; Kitamura, T.; Wada, Y.; Yanagida, S. Influence of TiO$_2$ Nanoparticle Size on Electron Diffusion and Recombination in Dye-Sensitized TiO$_2$ Solar Cells. *J. Phys. Chem. B* **2003**, *107*, 8607−8611.

(36) Yip, C. T.; Liu, X.; Hou, Y.; Xie, W.; He, J.; Schlücker, S.; Dang Yuan Lei, D. Y.; Huang, H. Strong Competition Between Electromagnetic Enhancement and Surface-Energy-Transfer Induced Quenching in Plasmonic Dye-Sensitized Solar Cells: A generic yet controllable effect. *Nano Energy* **2016**, *26*, 297−304.

(37) He, J.; Zheng, W.; Ligmajer, F.; Chan, C.-F.; Bao, Z.; Wong, K.-L.; Chen, X.; Hao, J.; Dai, J.; Yu, S.-F.; Lei, D. Y. Plasmonic Enhancement and Polarization Dependence of Nonlinear Upconversion Emissions from Single Gold Nanorod@SiO$_2$@CaF$_2$: Yb^{3+}, Er^{3+} Hybrid Core-Shell-Satellite Nanostructures. *Light Sci. Appl.* **2017**, *6*, No. e16217.

(38) Ou, W.; Zhou, B.; Shen, J.; Lo, T. W.; Lei, D.; Li, S.; Zhong, J.; Li, Y. Y.; Lu, J. Thermal and Nonthermal Effects in Plasmon-Mediated Electrochemistry at Nanostructured Ag Electrodes. *Angew. Chem., Int. Ed.* **2020**, *59*, 6790−6793.

(39) Zhou, L.; Swearer, D. F.; Zhang, C.; Robatjazi, H.; Zhao, H.; Henderson, L.; Dong, L.; Christopher, P.; Carter, E. A.; Nordlander, P.; Halas, N. J. Quantifying Hot Carrier and Thermal Contributions in Plasmonic Photocatalysis. *Science* **2018**, *362*, 69−72.